

$1/f^\alpha$ power spectrum in the Kardar-Parisi-Zhang universality class

Kazumasa A Takeuchi

Department of Physics, Tokyo Institute of Technology,
2-12-1 Ookayama, Meguro-ku, Tokyo 152-8551, Japan.

E-mail: kat@kaztake.org

Abstract. The power spectrum of interface fluctuations in the $(1+1)$ -dimensional Kardar-Parisi-Zhang (KPZ) universality class is studied both experimentally and numerically. The $1/f^\alpha$ -type spectrum is found and characterized through a set of “critical exponents” for the power spectrum. The recently formulated “aging Wiener-Khinchin theorem” accounts for the observed exponents. Interestingly, the $1/f^\alpha$ spectrum in the KPZ class turns out to contain information on a universal distribution function characterizing the asymptotic state of the KPZ interfaces, namely the Baik-Rains universal variance. It is indeed observed in the presented data, both experimental and numerical, and for both circular and flat interfaces, in the long time limit.

Keywords: power spectrum, $1/f$ noise, Kardar-Parisi-Zhang universality class

1. Introduction

The power spectrum[‡]

$$S(\omega; T) = \frac{1}{T} \left| \int_0^T X(t) e^{-i\omega t} dt \right|^2 \quad (1)$$

is a useful tool to characterize fluctuating signals $X(t)$ in general. Curiously, there have been reported a vast variety of systems showing a power law in $S(\omega)$ at low frequencies,

$$S(\omega) \sim 1/\omega^\alpha \quad (0 < \alpha < 2) \quad (2)$$

ranging from solid-state physics (vacuum tubes, semiconductors, etc.) [1–3] to fluid mechanics (e.g., turbulence), life science (e.g., heart beats) and other branches of science and technology [3, 4]. While the generic term “ $1/f$ noise” or more generically “ $1/f^\alpha$ noise” was coined to this phenomenon, various underlying mechanisms have been proposed in the literature.

Theoretical approaches to the $1/f^\alpha$ noise can be classified, roughly, into those based on *stationary* processes and on non-stationary, or *aging* ones. Here the stationarity indicates that the correlation function, defined with the ensemble average

$$C(\tau; t) = \langle X(t + \tau) X(t) \rangle, \quad (3)$$

[‡] In this paper, parameters of a function may be specified after its arguments, separated by a semicolon. These parameters may be dropped for simplicity.

does not depend on t . In this case the power spectrum $S(\omega; T)$ is a function of ω solely, and becomes simply the Fourier transform of $C(\tau)$, thanks to the celebrated Wiener-Khinchin theorem [5]. Since this simplifies analysis, and also because other kinds of noise such as Johnson-Nyquist noise and shot noise [6] have been successfully described under the assumption of stationarity, the same assumption has also been often adopted in models of $1/f^\alpha$ noise for solid-state systems [1, 2]. On the other side, recent experiments have shown examples of $1/f^\alpha$ noise in intermittent systems, such as blinking quantum dots [7–10] and nanoscale electrodes [11], which were shown to be non-stationary, or *aging*. The $1/f^\alpha$ noise in those systems was accounted for by models based on the intermittent dynamics [10–12], and the same line of analysis was also applied to turbulent fluid [13, 14] and fluctuating electroconvection of liquid crystal [15]. More generally, since the power law (2) would naturally suggest scale invariance in time scales, $1/f^\alpha$ noise is widely expected in scale-invariant processes such as coarsening [16], self-organized criticality [17, 18], and growth processes [19], all of which are examples of aging systems. The Wiener-Khinchin theorem cannot be used in aging systems, but recently an analogous relationship between the correlation function and the power spectrum was derived for aging systems, named the “aging Wiener-Khinchin theorem” [20–22].

In this work, taking an example of scale-invariant fluctuations of growing interfaces, we characterize the power spectrum by a set of recently proposed “critical exponents” [10, 20–22]. This analysis has an advantage that one does not make any *a priori* assumption about the stationarity; instead, with the obtained exponents, one can judge whether the system is stationary or not, and, if aging is there, determine its time dependence. For the systems we study here, the observed exponents indeed indicate the relevance of aging, and they are successfully accounted for by the aging Wiener-Khinchin theorem. Moreover, this theorem turns out to unveil certain universal fluctuation property of the studied systems, namely the universal variance of the Baik-Rains distribution [23] for the Kardar-Parizi-Zhang (KPZ) universality class [19, 24–27]. This demonstrates that, at least in the problem of growing interfaces, the aging Wiener-Khinchin theorem can be used as a practical tool to characterize the systems of interest.

The paper is organized as follows. Section 2 is devoted to a brief introduction of growing interface fluctuations and the KPZ class, with some emphasis on remarkable theoretical developments attained for the (1+1)-dimensional case. The systems to study, either experimentally or numerically, are described in section 3. The results on the power spectrum, characterized through the critical exponents and the aging Wiener-Khinchin theorem, are presented in section 4. Concluding remarks are given in section 5.

2. Growing interfaces and KPZ

When a system consists of two regions bordered by a well-defined interface, and if one of the two regions expands in a fluctuating manner, the interface typically develops intricate winding structure (see, e.g., figure 1ab). Examples abound from physics to

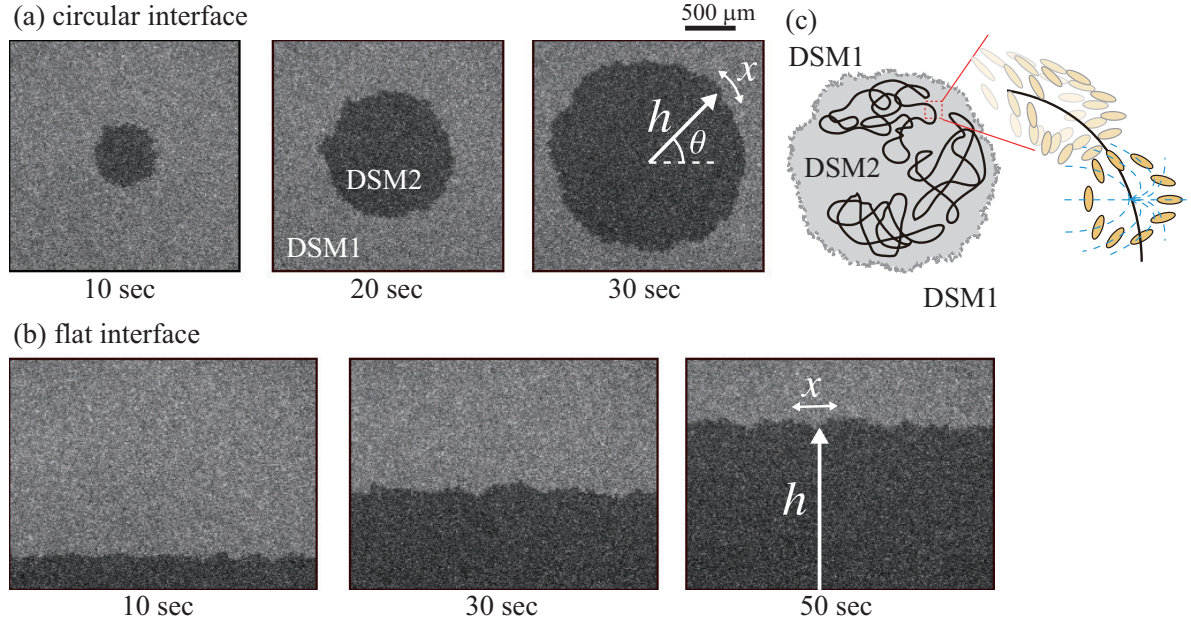


Figure 1. Growing interfaces in liquid-crystal turbulence [28–30], separating an expanding DSM2 region (black) and the surrounding DSM1 region (gray). See section 3.1 for descriptions of the experimental system and the DSM1/DSM2 turbulence. Starting from a point DSM2 nucleus, one obtains a circular interface (a), while from a line a flat interface is generated (b). The time is measured from the emission of laser pulses used to trigger DSM2. See also Supplementary Movies of reference [29]. (c) Sketch of the DSM1 and DSM2 states. DSM2 consists of a large density of line defects, specifically disclinations, in the liquid-crystal director field. The panels (a) and (b) were reprinted with adaptation from Fig. 3(a) of reference [30] and the panel (c) from Fig. 1(b) of the same reference, with permission of Springer.

biology and chemistry, as well as from nanoscales to macroscales, including surfaces of deposited solid films [31, 32], growing clusters of liquid-crystal turbulence [28–30], fronts of smoldering papers [33, 34], expanding colony of bacteria [35], propagation of chemical waves in disordered flow [36], etc. (see also [19, 37]). Interestingly, the observed patterns are generically scale-invariant, without fine tuning of experimental conditions and/or parameters [19]: in terms of the local height of interface, $h(x, t)$, as a function of lateral coordinates x and time t (figure 1ab)§, its fluctuation $\delta h(x, t) \equiv h(x, t) - \langle h(x, t) \rangle$ is statistically invariant under certain set of coordinate rescaling, $t \rightarrow bt$, $x \rightarrow b^{1/z}x$, $\delta h \rightarrow b^\beta \delta h$. This is analogous to dynamic critical behavior, with β and z playing the role of the critical exponents and $h(x, t)$ being the order parameter. As a result, such growing interfaces may be described by a set of universal scaling laws, with the critical exponents and scaling functions specific to each universality class. The KPZ class is one such universality class, known to describe the simplest generic case [19], with a variety

§ Note that, for the circular interfaces (e.g., figure 1a), the lateral coordinate is more appropriately specified by the azimuth θ , which remains constant along the mean growth direction. With this, the coordinate x (of dimension of length) can be formally defined by $x = R(t)\theta$, using mean radius $R(t)$ at time t .

of examples from theoretical models and experiments; in fact, the above-mentioned experiments were all shown to be in the KPZ class, at least in some parameter space and with the materials chosen in the studies^{||}.

Recently, the KPZ class became crucial in the studies of non-equilibrium scaling laws, when it turned out to be analytically tractable in many aspects for the $(1+1)$ -dimensional case [25–27], i.e., for one-dimensional interfaces growing in two-dimensional space. In this case, the scaling exponents are known to be $z = 3/2$ and $\beta = 1/3$ [19, 24]; the fluctuation amplitude increases as $\delta h \sim t^{1/3}$, with the lateral correlation length $\xi \sim t^{2/3}$. The height $h(x, t)$ grows, therefore, as

$$h(x, t) \simeq v_\infty t + (\Gamma t)^{1/3} \chi_{x,t}, \quad (4)$$

with constant parameters v_∞, Γ and a rescaled random variable $\chi_{x,t}$, which carries all relevant information of KPZ interface fluctuations. The recent theoretical developments then provided exact solutions for the one-point distribution of $\chi_{x,t}$, as well as its spatial correlation, revealing surprising link to random matrix theory, combinatorics, and quantum integrability [25–27, 38]. Remarkably, the results turned out to be classified into a few *universality subclasses* [38], determined by the global geometry of interfaces, or equivalently by the initial condition (table 1). For circular interfaces growing from a point nucleus (figure 1a and figure 2b), the asymptotic distribution is given by the Tracy-Widom distribution for the Gaussian unitary ensemble (GUE), originally introduced to describe fluctuations of the largest eigenvalue of GUE random matrices [39]; in other words, $\chi_{x,t} \xrightarrow{d} \chi_2$, where “ \xrightarrow{d} ” denotes convergence in the distribution and χ_2 is the standard random variable for the GUE Tracy-Widom distribution. This case is called the circular subclass, a subset of the KPZ class for circular interfaces. Similarly, the flat subclass describes globally flat interfaces starting from a straight line (figure 1b). It is characterized by the Tracy-Widom distribution for the Gaussian orthogonal ensemble (GOE) [40], or more precisely, $\chi_{x,t} \xrightarrow{d} \chi_1$ with χ_1 being the GOE Tracy-Widom variable multiplied by $2^{-2/3}$ [38]. Another established subclass is associated with the Brownian initial condition, i.e., $h(x, 0) = B_x$ with Brownian motion B_t , which is known to coincide with the asymptotic profile of interfaces in the $(1+1)$ -dimensional KPZ class [19][¶]. This subclass is then characterized by another distribution called the Baik-Rains distribution [23] ($\chi_{x,t} \xrightarrow{d} \chi_0$). The spatial correlation was also solved, and given by time correlation of certain stochastic process, called the Airy_2 , Airy_1 , and $\text{Airy}_{\text{stat}}$ process for the circular, flat, and Brownian subclass, respectively [25–27]. While other subclasses may also exist, these three are the main subclasses constituting the $(1+1)$ -dimensional KPZ

^{||} There also exist many experimental examples of growing interfaces that are *not* in the KPZ class [19, 37]. Although some of those systems have macroscopic ingredients that can generally affect the universality class, such as quenched disorder, it remains challenging to predict whether a given experimental system is in the KPZ class or not.

[¶] Therefore, this subclass is often called the “stationary subclass” in the literature, while here we call it the Brownian subclass, in order to avoid confusion with stationary processes. The diffusion coefficient of the Brownian motion B_t is chosen in such a way that it matches with that of the asymptotic interface profile.

Table 1. Three representative subclasses for the (1+1)-dimensional KPZ class [25–27].

| KPZ subclass | circular | flat | Brownian |
|---|---|--|------------------------------|
| initial condition ^a (typical) | $h(x, 0) = \begin{cases} 0 & (x = 0) \\ -\infty & (x \neq 0) \end{cases}$ (or point nucleus) | $h(x, 0) = 0$ | $h(x, 0) = B_x$ |
| exponents | $z = 3/2$ and $\beta = 1/3$ for all subclasses | | |
| distribution | GUE Tracy-Widom (χ_2) | GOE Tracy-Widom (χ_1) | Baik-Rains (χ_0) |
| (mean, var, s, k) ^b | (-1.77, 0.813, 0.224, 0.093) | (-0.760, 0.638, 0.293, 0.165) ^c | (0, 1.15, 0.359, 0.289) |
| spatial process | Airy ₂ process | Airy ₁ process | Airy _{stat} process |

^a The listed initial conditions are those typically used in the literature. Other conditions that share the same global symmetry are expected to lead to the same subclass.

^b Mean $\langle \chi_i \rangle$, variance $\langle \chi_i^2 \rangle_c$, skewness $\langle \chi_i^3 \rangle_c / \langle \chi_i^2 \rangle_c^{3/2}$ and kurtosis $\langle \chi_i^4 \rangle_c / \langle \chi_i^2 \rangle_c^2$ are shown, where $\langle \chi_i^n \rangle_c$ denotes the n th-order cumulant of χ_i . These are cited from [38], in which more precise values are given.

^c As noted in the main text, χ_1 differs from the usual definition of the GOE Tracy-Widom variable by the factor $2^{-2/3}$. The values of the cumulants change accordingly.

class, characterized by the same critical exponents, yet by the different non-Gaussian distributions and correlation functions.

In contrast to these remarkable developments on the distribution and spatial correlation functions [25–27], much less is known theoretically about the time correlation; analytical treatment of two-time quantities was made only very recently [41–43] and many other aspects of time correlation, in particular persistence properties, observed experimentally [30, 44] and numerically [44–47] remain to be explained. Here we aim to characterize how the local fluctuation of interface $\delta h(x, t)$ evolves in time, using the power spectrum and related analysis developed in the context of the $1/f^\alpha$ noise. Note that, while KPZ dynamics is clearly non-stationary, or aging, depending explicitly on time t measured from the start of the growth process, this non-stationarity will not be assumed *a priori* in the data analysis. Concerning the systems to study, we use the experiment on liquid-crystal turbulence [28–30] (figure 1; circular and flat cases), as well as an off-lattice version of the Eden model [47] (figure 2; circular case) and a discrete version of the polynuclear growth (PNG) model [48] (flat case), described in the following section. These models are not meant to describe the liquid-crystal turbulence, but studied instead to test universality of the results within the KPZ class.

3. Systems

3.1. Liquid-crystal turbulence

Nematic liquid crystal with negative dielectric anisotropy $\epsilon_{\parallel} < \epsilon_{\perp}$ and positive conductivity anisotropy $\sigma_{\parallel} > \sigma_{\perp}$ is known to develop convection, when confined between two plates and subjected to an alternating electric field with a relatively low

frequency, driven by the Carr-Helfrich effect [49]. Similarly to the thermal convection, this electroconvection undergoes a series of transitions in the convection pattern as the driving strength – the amplitude of the voltage applied to the system – increases. Eventually, the system reaches regimes of turbulence, or more precisely, spatiotemporal chaos, called the dynamic scattering modes (DSM) 1 and 2. They are distinct in the density of topological defects, specifically, disclinations, in the liquid-crystal director field (figure 1c): while DSM1 has no sustained disclinations, DSM2 consists of a large density of densely entangled disclinations. Therefore, DSM2 scatters light more strongly, hence looks darker in the transmitted light images (see figure 1). Under sufficiently high applied voltage, these disclinations are kept dense, stretched, and randomly transported by local turbulent flow of the electroconvection. This leads in macroscopic scales to fluctuating growth of the DSM2 region, which takes over the metastable DSM1 state (figure 1).

In our setup, detailed in the author’s past publication [30], the initial DSM2 region was generated by shooting ultraviolet laser pulses to the sample. If pulses are focused on a point, a DSM2 point nucleus is created, which then grows, forming a circular interface (figure 1a). If the laser beam profile is expanded along a line, longer than the width of the camera view field, DSM2 is generated on that line, producing a flat interface (figure 1b). This allows us to study both circular and flat interfaces under the practically same experimental conditions, each case repeated nearly one thousand times to achieve high statistical accuracy. For the applied voltage 26 V used here, the scaling coefficients were estimated to be $v_\infty = 33.24(4) \mu\text{m/s}$ and $\Gamma = 2.29(3) \times 10^3 \mu\text{m}^3/\text{s}$ for the circular case, and $v_\infty = 32.75(3) \mu\text{m/s}$ and $\Gamma = 2.15(10) \times 10^3 \mu\text{m}^3/\text{s}$ for the flat case [30], where the numbers in the parentheses indicate uncertainties in the last digit(s) of the estimates⁺. The circular and flat interfaces were found to show the hallmarks of the circular and flat KPZ subclasses, respectively, indicated in table 1. In the following, the applied voltage is fixed at 26 V, but as long as the voltage is within a reasonable range for studying growing DSM2 interfaces, we can expect the same results (under proper rescaling) at different voltages [30].

To evaluate the power spectrum (1), we use time series of $h(x, t)$ along the growth direction, i.e., with fixed θ for the circular case and fixed x for the flat case (see figure 1ab). Because the interfaces were not faithfully detected for the first few seconds from the laser emission, the time series were recorded for $t_{\min} \leq t \leq t_{\max}$, with $(t_{\min}, t_{\max}) = (2.0 \text{ s}, 30.5 \text{ s})$ for the circular case and $(t_{\min}, t_{\max}) = (3.0 \text{ s}, 63.0 \text{ s})$ for the flat case. Concerning the time resolution, all images taken during the above time periods were analyzed in the present study, so that the time interval Δt is 0.10 s for the circular case and 0.12 s for the flat case, improving the resolution used in the past work [30].

⁺ Although the parameters v_∞ and Γ are expected to be independent of the interface geometry, the experimentally obtained estimates were slightly different. This is presumably because of small uncontrolled shifts in the experimental conditions, during the period (8 days) between the two sets of the experiments.

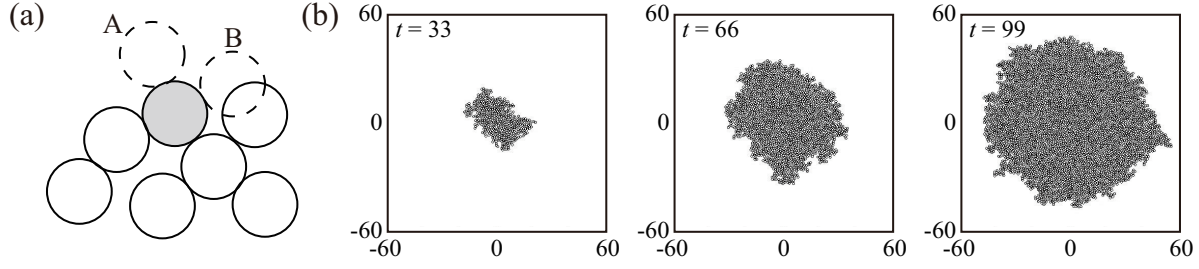


Figure 2. Off-lattice Eden model. (a) Evolution rule. Suppose the gray particle is chosen from $N_{\text{part}}(t)$ existing ones. Then we attempt to put a new particle, in an angular direction randomly chosen from $[0, 2\pi)$. If it does not overlap with other particles (such as the position A in the figure), the attempt is adopted, otherwise (such as the position B) it is withdrawn. (b) Typical evolution of an Eden cluster.

3.2. Off-lattice Eden model

To corroborate the experimental results obtained in the present work, we also investigate simple models of growing interfaces, which are known to be in the KPZ class. For the circular case, to attain better statistical accuracy, one needs an isotropically growing system so that the interface height $h(x, t)$ at all angular positions can be treated equally. For this reason, here we use the off-lattice Eden model introduced in [47]. This model deals with a cluster made of round particles of unit diameter, placed one by one in a two-dimensional space (figure 2a). Suppose there are $N_{\text{part}}(t)$ particles at time t . Then, at each time step, one chooses a particle randomly from them, and attempts to introduce a new particle next to it, in a direction chosen randomly in the two-dimensional plane. The new particle is placed if it does not overlap with any existing particle, otherwise the attempt is withdrawn. In any case, time t is increased by $1/N_{\text{part}}(t)$. Therefore, starting from a particle at the origin at $t = 0$, one obtains a growing cluster, bordered by an on average circular interface (figure 2b).

To speed up simulations, particles without empty adjacent space were excluded from the count of $N_{\text{part}}(t)$ (but still exist). Similarly, since we are only interested in the interface, particles left inside the outermost perimeter were also regularly excluded (see [47] for details). Time series were obtained from 100 independent realizations, in the range $t \leq t_{\text{max}} = 50000$ with resolution $\Delta t = 1$. For the scaling coefficients, we use $v_\infty = 0.51371$ and $\Gamma = 1.00$, taking the estimates from extensive simulations reported in [50].

3.3. Discrete PNG model

For the flat case, since we do not need isotropic growth, a lattice model is more convenient and fast to simulate. Here we use a discrete version of the PNG model with checkerboard updating, defined as follows. In this model, the height $h(x, t)$ is integer, and both x and t are discretized with step size δx and δt , respectively, i.e., $x = m\delta x$ and $t = n\delta t$ with integer m and n . Starting from the flat initial condition

$h(x, 0) = 0$, the height is updated by

$$h(x, t + \delta t) = \max\{h(x - \delta x, t), h(x, t), h(x + \delta x, t)\} + \eta(x, t), \quad (5)$$

where $\eta(x, t)$ is a random integer, independently drawn from the geometric distribution:

$$\text{Prob}[\eta(x, t) = k] = (1 - p)p^k \quad (k = 0, 1, 2, \dots) \quad (6)$$

The update is made only for odd sites at odd times and for even sites at even times, i.e., $\text{mod}(|n - m|, 2) = 0$. The advantage of this checkerboard updating is that the scaling coefficients are known exactly [48], specifically,

$$v_\infty = \frac{\sqrt{p}}{(1 - \sqrt{p})\delta t}, \quad \Gamma = \frac{\sqrt{p}(1 + \sqrt{p})}{2(1 - \sqrt{p})^3\delta t}. \quad (7)$$

By $\delta x = \delta t \rightarrow 0$ and $p = 2\rho\delta x\delta t$, one obtains the standard PNG model defined in continuous space and time, with nucleation rate ρ and step speed 1.

In the present work, we use $\delta x = \delta t = 0.1$ and $\rho = 2$. The lattice has 5×10^5 sites with the periodic boundary condition. Time series were recorded only at even time steps, hence the resolution is $\Delta t = 2\delta t = 0.2$. Simulations were carried out up to $t_{\max} = 10^6\delta t$ and 100 independent realizations were obtained.

4. Results

4.1. power spectrum and critical exponents

In the present work, we shall consider time series of two different quantities, both reflecting the local fluctuation of the height $h(x, t)$ at a fixed position (fixed x for the flat case and fixed θ for the circular case; see figure 1ab). The first quantity is the height fluctuation from the ensemble average*, $\delta h(x, t) \equiv h(x, t) - \langle h(x, t) \rangle$, which grows as $t^{1/3}$ (figure 3, top panels). The second quantity is the rescaled height, defined by

$$q(x, t) \equiv \frac{h(x, t) - v_\infty t}{(\Gamma t)^{1/3}} \simeq \chi_{x,t}, \quad (8)$$

which remains $\mathcal{O}(1)$ (figure 3, bottom panels) with a well-defined asymptotic distribution, i.e., $q \xrightarrow{d} \chi_i$ with $i = 1$ or 2 (see table 1). Consequently, we study the following two power spectra, averaged over x and realizations:

$$S_h(\omega; T) = \left\langle \frac{1}{N\Delta t} \left| \sum_{n=1}^N \delta h(x, t_n) e^{-i\omega t_n} \Delta t \right|^2 \right\rangle \quad (9)$$

and

$$S_q(\omega; T) = \left\langle \frac{1}{N\Delta t} \left| \sum_{n=1}^N q(x, t_n) e^{-i\omega t_n} \Delta t \right|^2 \right\rangle \quad (10)$$

with $t_n = t_{\min} + (n - 1)\Delta t$ ($t_{\min} = \Delta t$ for the simulations) \sharp , $t_N = T$, and ω being a multiple of $2\pi/N\Delta t$.

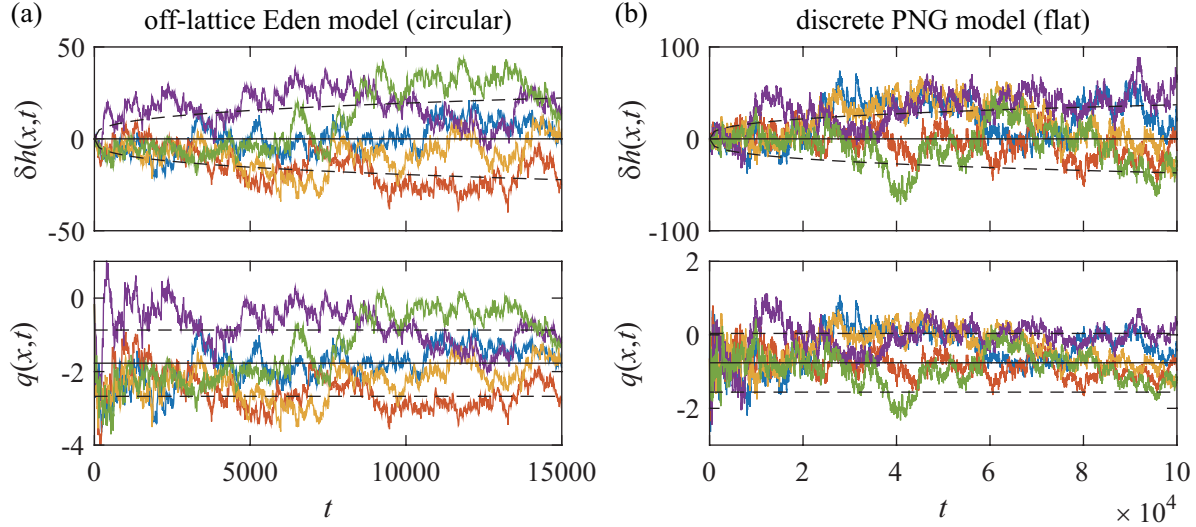


Figure 3. Typical time series of $\delta h(x, t)$ and $q(x, t)$ for the circular (a) and flat (b) cases. Numerical data are shown here, for which much longer time series are available. The solid and dashed black lines indicate the mean value and the range of the standard deviation, respectively, valid for large t . It is given by $\pm(\Gamma t)^{1/3} \sqrt{\langle \chi_i^2 \rangle_c}$ for $\delta h(x, t)$ and $\langle \chi_i \rangle \pm \sqrt{\langle \chi_i^2 \rangle_c}$ for $q(x, t)$, with $i = 2$ for the circular case and $i = 1$ for the flat case.

Figure 4 shows the power spectra $S_h(\omega; T)$ (panel a-d) and $S_q(\omega; T)$ (panel e-h) with different T , for both the experiments (a,b,e,f) and the simulations (c,d,g,h) and for both the circular case (a,c,e,g) and the flat case (b,d,f,h). In all cases, the power spectrum shows a power law at low frequencies, $S_h(\omega; T) \sim \omega^{-\alpha_h}$ and $S_q(\omega; T) \sim \omega^{-\alpha_q}$ with $\alpha_h = \alpha_q = 5/3$, hence the $1/f^\alpha$ -type spectrum is identified (see table 2 for the estimated exponent values). Moreover, while $S_h(\omega; T)$ does not depend on the measurement time T (figure 4a-d), $S_q(\omega; T)$ is found to decrease with increasing T (figure 4e-h). This may look somewhat counterintuitive if we recall $\delta h(x, t) \sim t^{1/3}$ and $q(x, t) \sim \mathcal{O}(1)$, but it can be clearly accounted for, as explained below.

To evaluate the T -dependence of $S_q(\omega; T)$, we seek for such a value of z_q that $S_q(\omega; T)T^{z_q}$ overlaps with different T (figure 5). While the experimental data seem to favor $z_q \approx 1/2$ within the limited observation time (figure 5a-d), the numerical data, obtained with much wider ranges of T , overlap reasonably well with $z_q \approx 2/3$ for large T (figure 5e,f and insets; see also table 2 for the estimates) and rule out $z_q = 1/2$ (figure 5g,h and insets). Indeed, since $q(x, t) \sim \mathcal{O}(1)$, the integrated power $\int_{2\pi/T}^\infty S_q(\omega; T) d\omega$ should remain finite for this process [4, 12, 22]; with $S_q(\omega; T) \sim T^{-z_q} \omega^{-\alpha_q}$, this condition implies $z_q = \alpha_q - 1 = 2/3$.

* Throughout section 4, the ensemble average $\langle \dots \rangle$ is obtained by averaging over realizations and spatial positions.

‡ Since aging processes do not have time translation symmetry, power spectrum in such processes depends not only on the measurement time T but also on the time to wait before the measurement, t_{\min} [12, 51]. Here we shall not consider this t_{\min} -dependence, because t_{\min} is fixed, taken as small as possible, and $t_{\min} \ll T$ is satisfied. Theoretically, the aging Wiener-Khinchin theorem that we shall use in this paper can be generalized for the case where t_{\min} is not negligible [52].

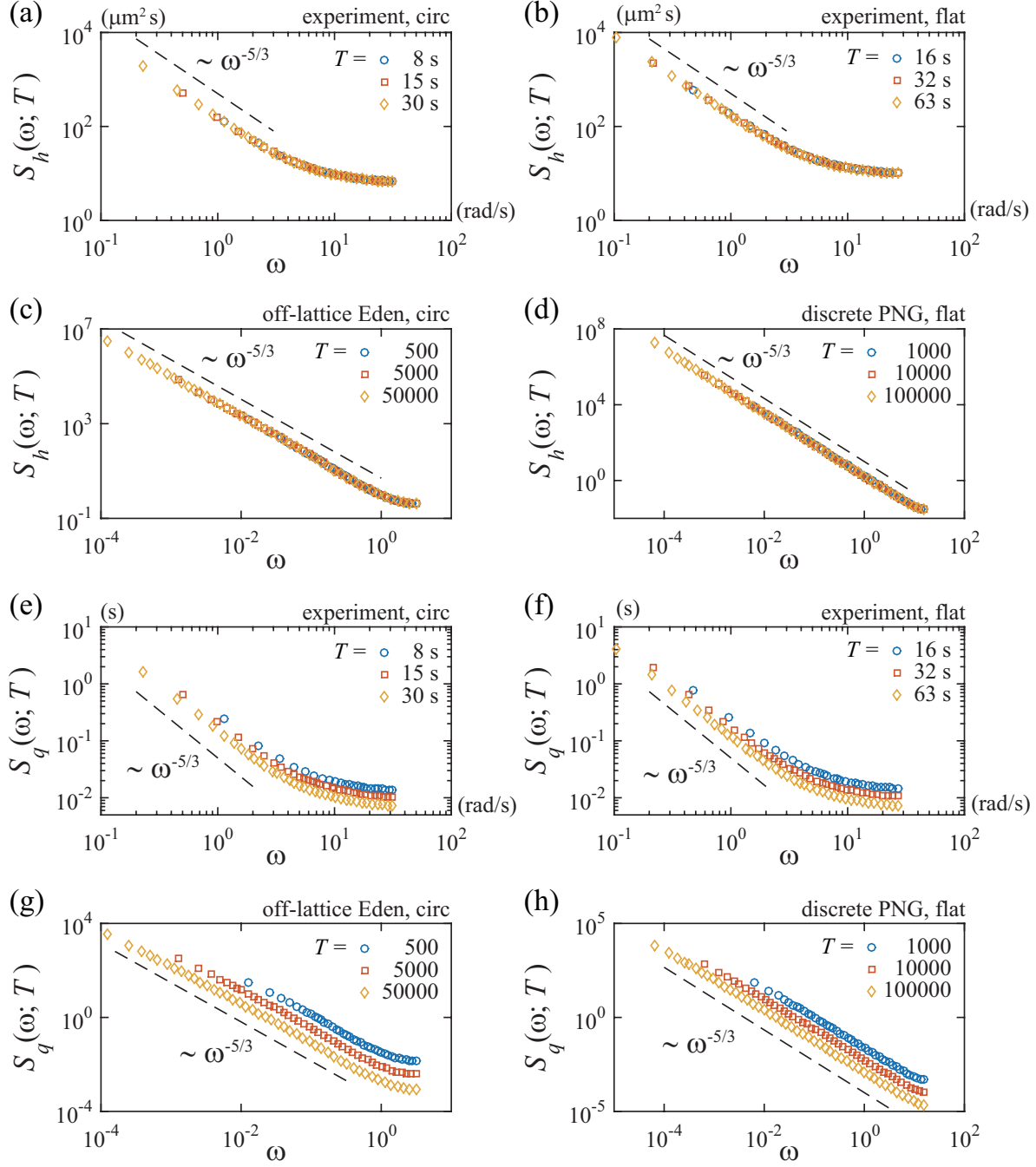


Figure 4. Power spectra $S_h(\omega; T)$ and $S_q(\omega; T)$ for the liquid-crystal experiments [circular (a,e), flat (b,f)], the off-lattice Eden model [circular (c,g)], and the discrete PNG model [flat (d,h)]. The dashed lines are guides for the eyes showing the power law $S_h(\omega; T) \sim \omega^{-5/3}$, $S_q(\omega; T) \sim \omega^{-5/3}$.

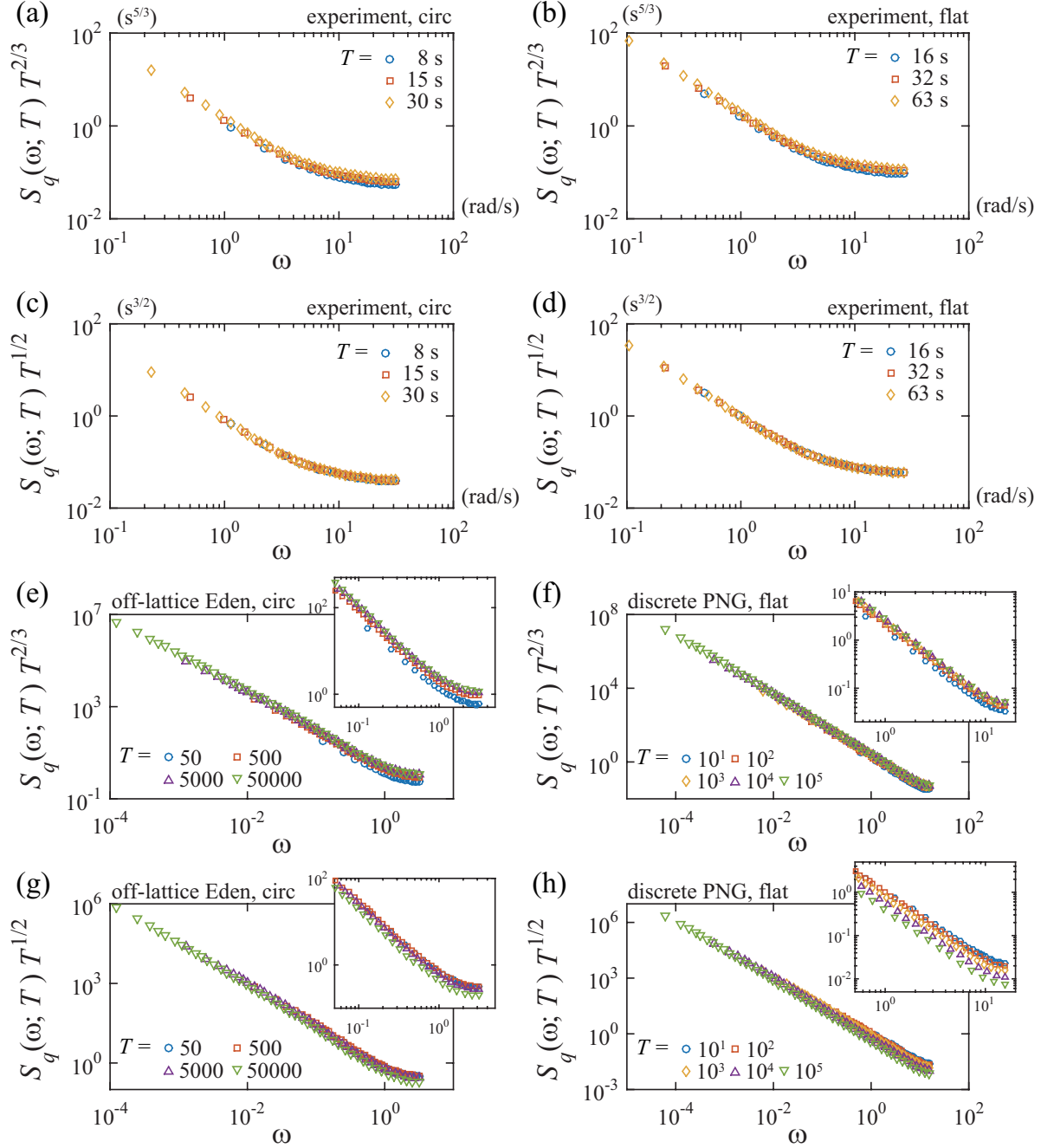


Figure 5. Evaluation of the aging exponent z_q for the power spectrum of the rescaled height, $S_q(\omega; T)$, for the liquid-crystal experiments [circular (a,c), flat (b,d)], the off-lattice Eden model [circular (e,g)], and the discrete PNG model [flat (f,h)]. The ordinates are $S_q(\omega; T)T^{z_q}$ with $z_q = 2/3$ (a,b,e,f) and $z_q = 1/2$ (c,d,g,h). For panels (e-h), the data are zoomed in and shown in the insets. Note that the data for large T (upright and inverted triangles) overlap with $z_q = 2/3$ (insets of e,f), but not with $z_q = 1/2$ (insets of g,h). See also table 2.

Further, recent studies [10, 20–22] proposed a set of critical exponents for the power spectrum. With $S_*(\omega; T)$ given by (1), where the subscript $*$ represents the choice of the variable $X(t)$, the exponents $(\alpha_*, z_*, \mu_*, \delta_*)$ are defined by:

$$\langle S_*(\omega; T) \rangle \sim T^{-z_*} \omega^{-\alpha_*} \quad (\text{for small } \omega) \quad (11)$$

and

$$\langle S_*(0; T) \rangle \sim T^{\mu_*}, \quad \Sigma_*(T) \equiv \int_{2\pi/T}^{\infty} \langle S_*(\omega; T) \rangle d\omega \sim T^{\delta_*}. \quad (12)$$

For our study, we define two sets of the exponents $(\alpha_h, z_h, \mu_h, \delta_h)$ and $(\alpha_q, z_q, \mu_q, \delta_q)$ for $S_h(\omega; T)$ and $S_q(\omega; T)$, respectively. The results in figures 4 and 5 then indicate $\alpha_h = \alpha_q = 5/3$, $z_h = 0$, and $z_q = 2/3$. For the exponents μ_* and δ_* , our data indicate $\mu_h = 5/3$, $\delta_h = 2/3$, $\mu_q = 1$, and $\delta_q = 0$ (figure 6 and table 2), though the experimental results for some exponents are not conclusive within the limit of the observation time.

4.2. Aging Wiener-Khinchin theorem

In fact, the exponents $(\alpha_*, z_*, \mu_*, \delta_*)$ we obtained can be accounted for by the recently formulated “aging Wiener-Khinchin theorem” [20–22]. Similarly to the standard Wiener-Khinchin theorem valid for stationary processes, the aging Wiener-Khinchin theorem describes relationship between the power spectrum $S_*(\omega; T)$ and the correlation function $C_*(\tau; t)$, defined by (1) and (3), respectively, for aging processes. Specifically, under the assumption that the correlation function $C(\tau; t)$ takes the form

$$C_*(\tau; t) \simeq t^{\Upsilon_*} \phi_*(\tau/t) \quad (13)$$

for large τ and t , which is usually satisfied in scale-invariant systems including the KPZ-class interfaces, the aging Wiener-Khinchin theorem states that the ensemble-averaged power spectrum $\langle S_*(\omega; T) \rangle$ is obtained by

$$\langle S_*(\omega; T) \rangle = \frac{2T^{\Upsilon_*+1}}{2 + \Upsilon_*} \int_0^1 d\zeta (1 - \zeta)^{\Upsilon_*} \phi_* \left(\frac{\zeta}{1 - \zeta} \right) {}_1F_2 \left[1 + \frac{\Upsilon_*}{2}; \frac{1}{2}, 2 + \frac{\Upsilon_*}{2}; -(\frac{\omega T \zeta}{2})^2 \right] \quad (14)$$

with the hypergeometric function ${}_1F_2[a; b_1, b_2; x]$ [20–22]. Then one can show that the exponents $(\alpha_*, z_*, \mu_*, \delta_*)$ are controlled by short-time behavior of $\phi_*(\tau/t)$, which can usually be expanded as

$$\phi_*(y) \simeq a_* - b_* y^{V_*} \quad (y \ll 1), \quad (15)$$

Table 2. Experimental and numerical estimates of the critical exponents^a.

| system ^b | α_h | z_h | μ_h | δ_h | α_q | z_q | μ_q | δ_q |
|---------------------|------------|-----------|-----------|------------|------------|---------|-------------|-------------|
| exp. (circular) | 1.69(3) | 0.02(4) | 1.69(3) | 0.63(2) | 1.61(5) | | ≈ 1 | ≈ 0 |
| exp. (flat) | 1.67(5) | 0.03(3) | 1.64(3) | 0.60(3) | 1.67(5) | | ≈ 1 | ≈ 0 |
| Eden (circular) | 1.67(2) | 0.00(3) | 1.68(3) | 0.67(2) | 1.61(9) | 0.63(3) | 1.02(4) | 0.01(3) |
| PNG (flat) | 1.672(15) | 0.010(15) | 1.664(13) | 0.667(13) | 1.64(2) | 0.64(4) | 1.00(2) | 0.001(12) |
| theory (table 3) | 5/3 | 0 | 5/3 | 2/3 | 5/3 | 2/3 | 1 | 0 |

^a The number in parentheses indicates a range of error in the last digit(s), evaluated within the observation time. The symbol \approx represents that the data are consistent with the indicated exponent value, but do not seem to reach the asymptotic time region during the observation time; consequently, the range of error could not be estimated reliably.

^b Abbreviations: exp. = liquid-crystal experiment, Eden = off-lattice Eden model, PNG = discrete PNG model.

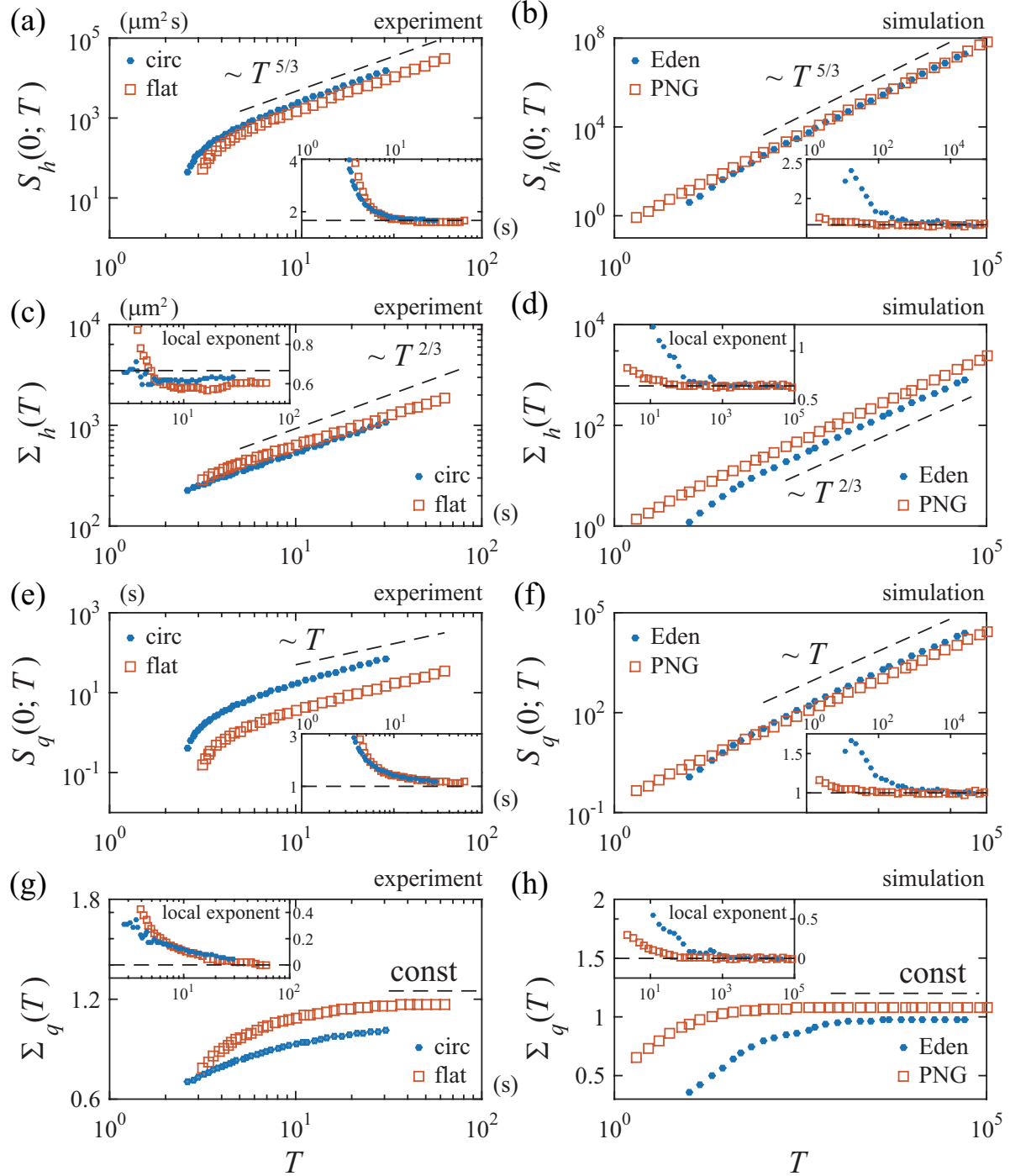


Figure 6. Evaluation of the exponents μ_* and δ_* for the liquid-crystal experiments (a,c,e,g) and for the simulations (b,d,f,h). Data for the circular and flat interfaces are shown in blue dots and red squares, respectively. The dashed lines are guides for the eyes indicating the exponent expected from the aging Wiener-Khinchin theorem. The insets show the local exponent $\frac{d(\log y)}{d(\log T)}$ against T , where y denotes the ordinates used in the main panels.

and obtain the following scaling relations [22]:

$$\begin{aligned}\alpha_* &= 1 + V_*, & z_* &= V_* - \Upsilon_*, \\ \mu_* &= 1 + \Upsilon_*, & \delta_* &= \max\{-z_*, \mu_* - 1\}.\end{aligned}\tag{16}$$

For the KPZ class, with time series $X(t) = \delta h(x, t)$ or $q(x, t)$, we have [53]

$$\Upsilon_h = 2\beta = 2/3, \quad \Upsilon_q = 0, \quad V_h = V_q = 2\beta = 2/3,\tag{17}$$

where we used $\beta = 1/3$ for the $(1+1)$ -dimensional case. With (16) and (17), we obtain the values of $(\alpha_h, z_h, \mu_h, \delta_h)$ and $(\alpha_q, z_q, \mu_q, \delta_q)$ as summarized in table 3, which are consistent with all the observations presented in figures 4-6 and table 2.

4.3. $1/f^\alpha$ spectrum and the Baik-Rains universal variance

In addition to the exponents, the aging Wiener-Khinchin theorem (14) also gives the coefficient C_* of the $1/f^\alpha$ spectrum [20–22], $\langle S(\omega; T) \rangle \simeq C_* T^{-z_*} \omega^{-\alpha_*}$ with $\omega T \gg 1$, by

$$C_* = \frac{2b_* \sin(\pi V_*/2) \Gamma(1 + V_*)}{1 + \Upsilon_* - V_*},\tag{18}$$

with the gamma function $\Gamma(\cdot)$. The condition $\omega T \gg 1$ implies that the time scale of interest, ω^{-1} , is much smaller than the observation time T , albeit larger than any microscopic time scale of the system.

Interestingly, for KPZ, this condition is exactly what one would need for the Brownian subclass [41, 43, 53, 54]. Starting from an arbitrary initial condition, we wait for long time T , so that the interface profile $h(x, T)$ becomes sufficiently close to the asymptotic profile, or Brownian motion, B_x (see section 2). Now we regard $h(x, T)$ as a new initial condition and consider the relative height $h'(x, t') = h(x, T + t') - h(x, T)$, then $h'(x, t')$ evolves as in (4) and the corresponding random variable $\chi'_{x, t'}$ exhibits the universal properties of the Brownian KPZ subclass, as long as $t' \ll T$ [27, 41, 43, 54, 55]. Indeed, with $C_h(\tau; t) = \langle \delta h(t + \tau) \delta h(t) \rangle$ and $\phi_h(\tau/t)$ defined by (13) accordingly, we can show, for $\tau/t \rightarrow 0$,

$$\phi_h(\tau/t) \simeq \Gamma^{2/3} \left[\langle \chi_i^2 \rangle_c - \frac{1}{2} \langle \chi_0^2 \rangle_c (\tau/t)^{2/3} + \mathcal{O}(\tau/t) \right].\tag{19}$$

Here, $\chi_i = \chi_2$ or χ_1 depending on the initial condition (circular or flat, respectively) and $\langle \cdot^2 \rangle_c$ denotes the variance; hence $\langle \chi_0^2 \rangle_c$ is the variance of the Baik-Rains distribution, a universal hallmark of the Brownian KPZ subclass (table 1). Comparing (19) with (15),

Table 3. Critical exponents for the $(1+1)$ -dimensional KPZ class.

| time series | Υ_* | V_* | α_* | z_* | μ_* | δ_* |
|--------------------------------------|--------------|-------|------------|-------|---------|------------|
| height fluctuations $\delta h(x, t)$ | 2/3 | 2/3 | 5/3 | 0 | 5/3 | 2/3 |
| rescaled height $q(x, t)$ | 0 | 2/3 | 5/3 | 2/3 | 1 | 0 |

we obtain $b_h = \frac{1}{2}\Gamma^{2/3}\langle\chi_0^2\rangle_c$. Therefore, using (18) with $V_h = \Upsilon_h = 2/3$, we finally arrive at

$$S_h(\omega; T) \simeq \langle\chi_0^2\rangle_c C'_h \omega^{-5/3}, \quad C'_h = \frac{\sqrt{3}}{2}\Gamma(5/3)\Gamma^{2/3}. \quad (20)$$

In other words, the coefficient of the $1/f^\alpha$ spectrum turns out to be the universal Baik-Rains variance, times a constant factor C'_h .

This is tested in figure 7, where $S_h(\omega; T)\omega^{5/3}/C'_h$ is plotted against ω and compared with $\langle\chi_0^2\rangle_c$. For the experimental circular interfaces, we find remarkable agreement (figure 7a); from the local minimum of the plateau, we obtain 1.151(12), very close to the Baik-Rains variance $\langle\chi_0^2\rangle_c = 1.15039$ [38]. For the other three cases (figure 7b-d), in contrast, we find some deviations from $\langle\chi_0^2\rangle_c$, which however decrease with increasing T . The deviations are found to decay by some power law T^{-a} , with exponent a compatible in the range $1/6 \lesssim a \lesssim 1/3$. From the PNG data, $a \approx 1/4$ is suggested, but data for other systems and for longer observation times are needed to make a conclusion about the value of this exponent. In any case, all the results presented in figure 7 indeed support the validity of (20) in the asymptotic limit; the coefficient of the $1/f^\alpha$ spectrum is essentially the Baik-Rains universal variance.

Our result indicates that, if the relative height $h'(x, t') = h(x, T + t') - h(x, T)$ with $t' \ll T$ is considered, circular and flat KPZ interfaces indeed approach the Brownian subclass. This crossover has been known for the flat interfaces [27, 41, 54, 55], but to the knowledge of the author it is first shown here for the circular case, apart from indirect evidence in [43], in agreement with theoretical predictions [41, 43]. Curiously, by direct analysis of the relative height $h'(x, t')$, using the liquid-crystal experimental data for the flat case, the variance of the rescaled relative height remained far from the Baik-Rains variance within the observation time [54], which is also the time used in the present study. As shown here, for this experimental system, the power spectrum exhibits the Baik-Rains signature much earlier, by simpler analysis. On the other hand, the earlier work [54] also used a discrete PNG model^{††}, for which the Baik-Rains variance was more easily found in the relative height $h'(x, t')$ than in the power spectrum shown in the present paper. Indeed, the relative height method has been usually used in numerical studies and provided good estimates of the Baik-Rains variance [27, 53–56]. Since the two methods seem to have different strengths of the finite-time effect, it would be useful to measure both the relative height and the power spectrum. Note that the power spectrum method can also be used for higher dimensions, for which the counterpart of the Baik-Rains distribution is not solved analytically. For $2 + 1$ dimensions, numerical [57] and non-exact theoretical [58] estimates are available; it would be then interesting to compare the power-spectrum method with these known results.

^{††}The discrete PNG model studied in [54] was defined with the synchronous update, while in the present paper we used the checkerboard update. The author also measured the power spectrum $S_h(\omega; T)$ in the case of the synchronous update, and found a result similar to figure 7.

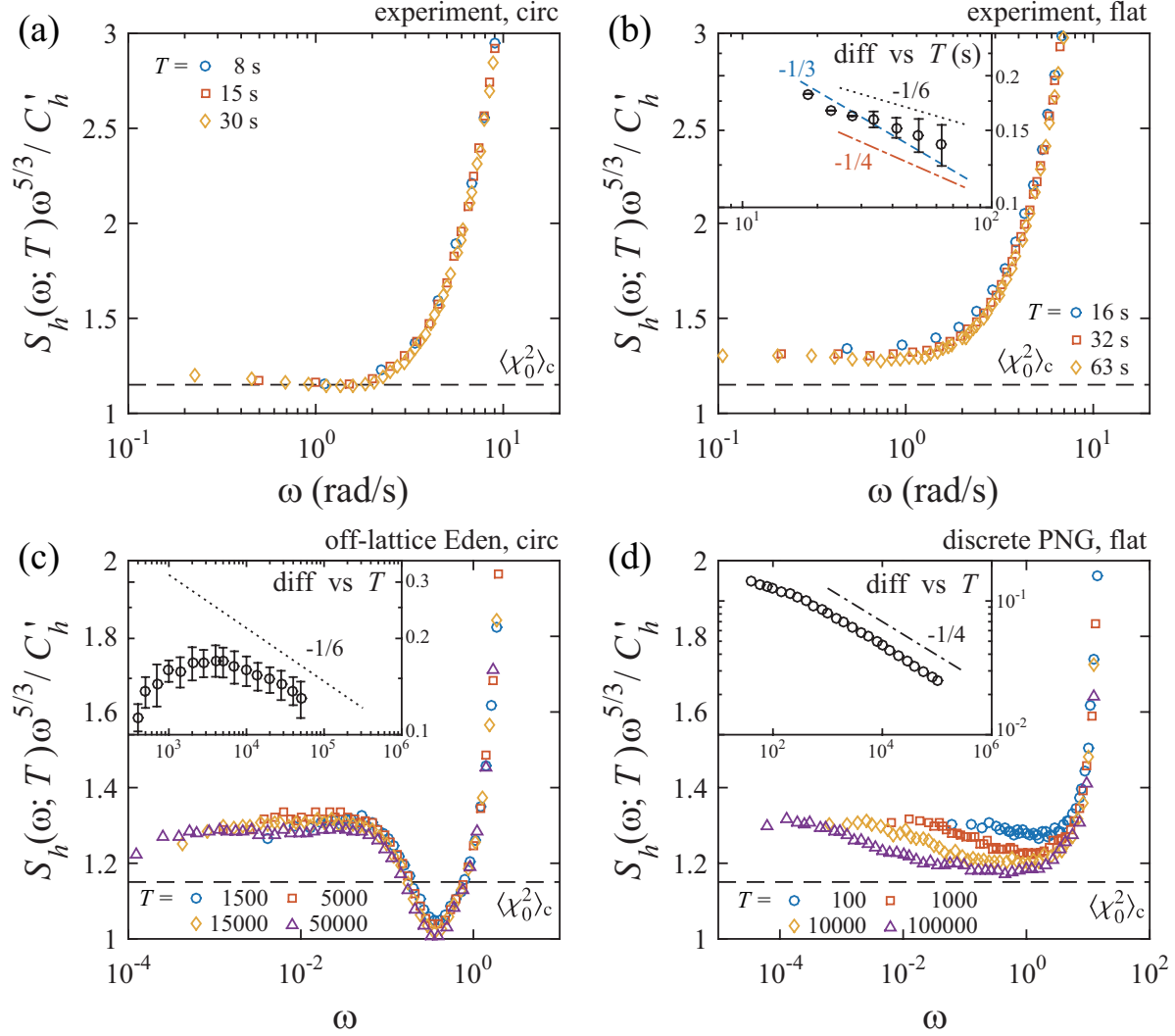


Figure 7. Comparison of the coefficient of the $1/f^\alpha$ spectrum with the Baik-Rains universal variance, for the liquid-crystal experiments [circular (a), flat (b)], the off-lattice Eden model [circular (c)], and the discrete PNG model [flat (d)]. According to the aging Wiener-Khinchin theorem and the KPZ scaling laws, the ordinate $S_h(\omega; T)\omega^{5/3}/C'_h$ is expected to converge to the Baik-Rains variance $\langle \chi_0^2 \rangle_c$ for $T^{-1} \ll \omega \ll \min\{\Delta t^{-1}, \tau_0^{-1}\}$, where Δt is the time resolution and τ_0 is a microscopic time scale of the system (see (20)). The dashed lines indicate $\langle \chi_0^2 \rangle_c = 1.15039$. In the insets, the difference between $S_h(\omega; T)\omega^{5/3}/C'_h$ and $\langle \chi_0^2 \rangle_c$ is plotted as a function of T . The difference is measured from the value of the plateau region of the main-panel data for (b,c), with errorbars indicating the minimum and maximum in that region; for (d) the difference is measured from the local minimum estimated by cubic fitting. The dotted, dashed-dotted, and dashed lines are guides for the eyes, indicating exponents $-1/6$, $-1/4$, and $-1/3$, respectively.

5. Concluding remarks

In this paper, we have studied the $1/f^\alpha$ -type power spectrum of interface fluctuations in the $(1+1)$ -dimensional KPZ class, both experimentally and numerically, using the liquid-crystal turbulence as well as simple models, specifically, the off-lattice Eden model and the discrete PNG model. We measured the power spectrum for two different sets of time series, namely those for the height fluctuation $\delta h(x, t)$ and the rescaled height $q(x, t)$, and characterized it by a set of critical exponents (figures 4-6 and table 2). The observed exponents were found to be in good agreement with predictions (16) and (18) from the recently proposed, aging Wiener-Khinchin theorem [20–22]. Moreover, this theory revealed that the coefficient of the $1/f^\alpha$ spectrum contains essential information on the universal properties of the asymptotic KPZ interfaces, namely the Baik-Rains universal variance, through (20). This intriguing connection was corroborated by both experimental and numerical data (figure 7). In relation to the KPZ universality subclass (table 1), our results constitute experimental and numerical supports that the relative height $h'(x, t') = h(x, T + t') - h(x, T)$ of circular and flat interfaces belongs to the Brownian KPZ subclass in the asymptotic limit $t'/T \rightarrow 0$ with $t', T \rightarrow \infty$. On the other hand, the power spectrum does not seem to be as efficient for studying time correlation properties in the other limit $t'/T \rightarrow \infty$, which characterize the subclass for the bare height $h(x, t)$ (i.e, circular or flat in our case) and are known to be different between the two cases, even qualitatively [30, 41, 44].

From broader perspectives, it may be worth making a few general remarks about the power spectrum and the stationarity, which are not new but sometimes overlooked in the literature. First, one should recall that the stationarity in the power spectrum ($z_* = 0$) does not necessarily imply the stationarity of the underlying process, neither the boundedness of the time series; this is well-known from examples like the Brownian motion and reminded here in figure 4a-d, where $S_h(\omega; T)$ does not depend on T but the process $\delta h(x, t)$ is aging and unbounded. The stationarity of the process can be inferred instead by measuring in addition the “power” at zero frequency, $\langle S(0; T) \rangle = T \langle \bar{X}^2 \rangle$ with $\bar{X} = \frac{1}{T} \int_0^T X(t) dt$, which is either linear in T (if $\bar{X} \neq 0$) or constant (if $\bar{X} = 0$) for stationary processes, while in the aging case it grows with a nontrivial exponent $\mu_* = \alpha_* - z_*$. Consistency with the aging scenario can be checked further through the set of the scaling relations (16) from the aging Wiener-Khinchin theorem [20–22]. It is also important to remark that, in aging systems, time average and ensemble average are in general different [12, 20–22]; while the present work focused on the ensemble average, a different form of the aging Wiener-Khinchin theorem should be used if one aims to connect to the time-averaged correlation function. Since aging seems to occur rather often in systems showing $1/f^\alpha$ noise, neither the equivalence between ensemble average and time average nor the usual Wiener-Khinchin theorem should be used unless firm evidence of stationarity is obtained. From this perspective, measuring the exponents $(\alpha_*, z_*, \mu_*, \delta_*)$ is a versatile approach that does not require any assumption on aging or stationarity, yet useful to characterize underlying processes, as shown for the example

of the KPZ class we studied here. It is hoped that this approach will also help to study other examples of the $1/f^\alpha$ -type spectrum, reported in the wealth of physical systems [1–4].

Acknowledgments

The author wishes to thank E. Barkai, A. Dechant, and T. Halpin-Healy for their enlightening discussions, as well as critical reading of the manuscript by R. A. L. Almeida, E. Barkai, A. Dechant, and T. Halpin-Healy. The author acknowledges financial support by KAKENHI from JSPS, Nos. JP25103004, JP16H04033, JP16K13846.

References

- [1] Dutta P and Horn P M 1981 *Rev. Mod. Phys.* **53** 497–516
- [2] Wong H 2003 *Microelectronics Reliability* **43** 585–599
- [3] Musha T, Sato S and Yamamoto M (eds) 1992 *Noise in Physical Systems and $1/f$ Fluctuations* (Tokyo: IOS Press)
- [4] Mandelbrot B B 1999 *Multifractals and $1/f$ Noise* (Berlin: Springer)
- [5] Kubo R, Toda M and Hashitsume N 1991 *Statistical Physics II, Nonequilibrium Statistical Mechanics* 2nd ed (Berlin: Springer)
- [6] Kobayashi K 2016 *Proc. Jpn. Acad. B* **92** 204–221
- [7] Pelton M, Grier D G and Guyot-Sionnest P 2004 *Appl. Phys. Lett.* **85** 819–821
- [8] Pelton M, Smith G, Scherer N F and Marcus R A 2007 *Proc. Natl. Acad. Sci. USA* **104** 14249–14254
- [9] Frantsuzov P A, Volkán-Kacsó S and Jankó B 2013 *Nano Lett.* **13** 402–408
- [10] Sadegh S, Barkai E and Krapf D 2014 *New J. Phys.* **16** 113054
- [11] Krapf D 2013 *Phys. Chem. Chem. Phys.* **15** 459–465
- [12] Niemann M, Kantz H and Barkai E 2013 *Phys. Rev. Lett.* **110** 140603
- [13] Herault J, Pétrélis F and Fauve S 2015 *Europhys. Lett.* **111** 44002
- [14] Herault J, Pétrélis F and Fauve S 2015 *J. Stat. Phys.* **161** 1379–1389
- [15] Silvestri L, Fronzoni L, Grigolini P and Allegrini P 2009 *Phys. Rev. Lett.* **102** 014502
- [16] Bray A J 1994 *Adv. Phys.* **43** 357–459
- [17] Bak P, Tang C and Wiesenfeld K 1987 *Phys. Rev. Lett.* **59** 381–384
- [18] Turcotte D L 1999 *Rep. Prog. Phys.* **62** 1377–1429
- [19] Barabási A L and Stanley H E 1995 *Fractal Concepts in Surface Growth* (Cambridge: Cambridge Univ. Press)
- [20] Leibovich N and Barkai E 2015 *Phys. Rev. Lett.* **115** 080602
- [21] Dechant A and Lutz E 2015 *Phys. Rev. Lett.* **115** 080603
- [22] Leibovich N, Dechant A, Lutz E and Barkai E 2016 *Phys. Rev. E* **94** 052130
- [23] Baik J and Rains E M 2000 *J. Stat. Phys.* **100** 523–541
- [24] Kardar M, Parisi G and Zhang Y C 1986 *Phys. Rev. Lett.* **56** 889–892
- [25] Kriecherbauer T and Krug J 2010 *J. Phys. A* **43** 403001
- [26] Corwin I 2012 *Random Matrices Theory Appl.* **1** 1130001
- [27] Halpin-Healy T and Takeuchi K A 2015 *J. Stat. Phys.* **160** 794–814
- [28] Takeuchi K A and Sano M 2010 *Phys. Rev. Lett.* **104** 230601
- [29] Takeuchi K A, Sano M, Sasamoto T and Spohn H 2011 *Sci. Rep.* **1** 34
- [30] Takeuchi K A and Sano M 2012 *J. Stat. Phys.* **147** 853–890
- [31] Palasantzas G, Tsamouras D and De Hosson J T M 2002 *Surf. Sci.* **507–510** 357–361

- [32] Almeida R A L, Ferreira S O, Oliveira T J and Reis F D A A a 2014 *Phys. Rev. B* **89** 045309
- [33] Maunuksela J, Myllys M, Kähkönen O P, Timonen J, Provatas N, Alava M J and Ala-Nissila T 1997 *Phys. Rev. Lett.* **79** 1515–1518
- [34] Myllys M, Maunuksela J, Alava M, Ala-Nissila T, Merikoski J and Timonen J 2001 *Phys. Rev. E* **64** 036101
- [35] Wakita J i, Itoh H, Matsuyama T and Matsushita M 1997 *J. Phys. Soc. Jpn.* **66** 67–72
- [36] Atis S, Dubey A K, Salin D, Talon L, Le Doussal P and Wiese K J 2015 *Phys. Rev. Lett.* **114** 234502
- [37] Takeuchi K A 2014 *J. Stat. Mech.* **2014** P01006
- [38] Prähofer M and Spohn H 2000 *Phys. Rev. Lett.* **84** 4882–4885
- [39] Tracy C A and Widom H 1994 *Commun. Math. Phys.* **159** 151–174
- [40] Tracy C A and Widom H 1996 *Commun. Math. Phys.* **177** 727–754
- [41] Ferrari P L and Spohn H 2016 *SIGMA* **12** 074
- [42] Johansson K 2017 *Commun. Math. Phys.* **351** 441–492
- [43] De Nardis J, Le Doussal P and Takeuchi K A 2017 *Phys. Rev. Lett.* **118** 125701
- [44] Takeuchi K A and Akimoto T 2016 *J. Stat. Phys.* **164** 1167–1182
- [45] Kallabis H and Krug J 1999 *Europhys. Lett.* **45** 20–25
- [46] Singha S B 2005 *J. Stat. Mech.* **2005** P08006
- [47] Takeuchi K A 2012 *J. Stat. Mech.* **2012** P05007
- [48] Sasamoto T and Imamura T 2004 *J. Stat. Phys.* **115** 749–803
- [49] de Gennes P G and Prost J 1995 *The Physics of Liquid Crystals* 2nd ed (*International Series of Monographs on Physics* vol 83) (New York: Oxford Univ. Press)
- [50] Alves S G, Oliveira T J and Ferreira S C 2013 *J. Stat. Mech.* **2013** P05007
- [51] Bouchaud J P, Cugliandolo L F, Kurchan J and Mézard M 1997 Out of equilibrium dynamics in spin-glasses and other glassy systems *Series on Directions in Condensed Matter Physics* vol 12 (World Scientific) pp 161–223 arXiv:cond-mat/9702070
- [52] Leibovich N and Barkai E 2016 private communication.
- [53] Krug J, Meakin P and Halpin-Healy T 1992 *Phys. Rev. A* **45** 638–653
- [54] Takeuchi K A 2013 *Phys. Rev. Lett.* **110** 210604
- [55] Halpin-Healy T and Lin Y 2014 *Phys. Rev. E* **89** 010103
- [56] Tang L H 1992 *J. Stat. Phys.* **67** 819–826
- [57] Halpin-Healy T 2013 *Phys. Rev. E* **88** 042118
- [58] Kloss T, Canet L and Wschebor N 2012 *Phys. Rev. E* **86** 051124